NANO · MICRO small
www.small-journal.com

Multimodal Bubble Microrobot Near an Air–Water Interface

Leilei Wang, Li Chen, Xu Zheng, Zexiong Yu, Wenchao Lv, Minjia Sheng, Lina Wang, Pengcheng Nie, Hangyu Li, Dongshi Guan, and Haihang Cui**

The development of multifunctional and robust swimming microrobots working at the free air–liquid interface has encountered challenge as new manipulation strategies are needed to overcome the complicated interfacial restrictions. Here, flexible but reliable mechanisms are shown that achieve a remote-control bubble microrobot with multiple working modes and high maneuverability by the assistance of a soft air–liquid interface. This bubble microrobot is developed from a hollow Janus microsphere (JM) regulated by a magnetic field, which can implement switchable working modes like pusher, gripper, anchor, and sweeper. The collapse of the microbubble and the accompanying directional jet flow play a key role for functioning in these working modes, which is analogous to a "bubble tentacle." Using a simple gamepad, the orientation and the navigation of the bubble microrobot can be easily manipulated. In particular, a speed modulation method is found for the bubble microrobot, which uses vertical magnetic field to control the orientation of the JM and the direction of the bubble-induced jet flow without changing the fuel concentration. The findings demonstrate a substantial advance of the bubble microrobot specifically working at the air–liquid interface and depict some nonintuitive mechanisms that can help develop more complicated microswimmers.

1. Introduction

The swimming microrobots using biomimetic swimming strategies and microscale fluid dynamics have recently made great progress.[1] These untethered microtools can establish flexible interactions between the macro world and the micro fluid environment,[2] and have shown important applications in various fields where precise micromanipulation is needed, for example, drug delivery,[3] single cell manipulation,[4] and micromotor navigation.[5] Compared with the traditional micromanipulation methods using microneedles or micropipettes,[6] newly developed microrobots can accurately manipulate single micro-target with a smart and less invasive manner. Current directions of research are focusing on developing multifunctional and robust swimming microrobot that can be flexibly controlled in complicated working environment.

In practical applications, swimming microrobots prevalently encounter either soft or hard boundaries. New challenges thus arise for the swimming microrobots restricted by the boundary confinement effect, which need to be clarified for developing better manipulation strategies. The influence of the solid–liquid interface on the motion of microrobots have been recently investigated.[5,7] However, robust microrobots that are specifically designed to work near a soft air–liquid interface have hardly been achieved due to the involvement of more complicated mechanisms from the soft air–liquid interface.[8] Different from the solid–liquid interface, the air–liquid interface has a significant surface tension in micro-scale, and the surface capillary wave can be easily generated due to the deformation of the air–liquid interface. In addition, the presence of the air–liquid interface will change the hydrodynamics that dominate the propulsion of the microrobot and the transport of the fuel,[9] which causes some difficulties to precisely control the microrobot. Thus, a deeper understanding of the role of the free air–liquid interface is necessary for researchers who intend to manipulate floating or suspended microparticles whose density is relatively low. Developing a robust strategy for multifunctional microrobot that can efficiently work near the air–liquid interface is greatly welcome in novel microfabrication platform[10] and special medical microrobot for surgery.[3b,c,11]

Nature has provided ingenious examples of manipulating microparticles using bubbles, such as the directional launching of the spores by the fern sporangium[12] and the bubble catapult played by shrimps.[13] It is well known that microbubbles contain great energy due to a large surface tension. Utilizing the surface energy stored by the microbubbles is essential to

L. Wang, Z. Yu
School of Environmental and Municipal Engineering
Xi'an University of Architecture and Technology
Xi'an 710055, China

L. Wang, X. Zheng, P. Nie, H. Li, D. Guan
State Key Laboratory of Nonlinear Mechanics
Beijing Key Laboratory of Engineered Construction and Mechanobiology
Institute of Mechanics
Chinese Academy of Science
Beijing 100190, China
E-mail: zhengxu@lnm.imech.ac.cn

L. Chen, W. Lv, M. Sheng, L. Wang, H. Cui
School of Building Services Science and Engineering
Xi'an University of Architecture and Technology
Xi'an 710055, China
E-mail: cuihaihang@xauat.edu.cn

P. Nie, H. Li, D. Guan
School of Engineering Science
University of Chinese Academy of Sciences
Beijing 100049, China

The ORCID identification number(s) for the author(s) of this article can be found under https://doi.org/10.1002/smll.202203872.

DOI: 10.1002/smll.202203872

improve the driving efficiency of bubble-driven microrobots and provides powerful and flexible ways of manipulation.[14] However, using microbubble to manipulate micro-cargos, as a "soft" method to replace the conventional mechanical means, is a tricky problem in microrobotics. Recent progress has shown the capability of bubble microrobots to perform functions like gripping or propelling.[15] Ongoing efforts are being made to develop multifunctional bubble microrobot with higher controllability, which requires fast response under real-time control, high maneuverability, easy switch between different functions, and feasibility to work in complicated environments. These advances rely on better understanding and sophisticated manipulation of the bubble dynamics and the associated hydrodynamic effect near the free surface.

Herein, we present a remote-control bubble microrobot and demonstrate its multifunctional working modes of manipulating target micro-cargos near a free air–liquid interface (**Figure 1**). This bubble microrobot is composed of a Janus microsphere (JM), which serves as a microbubble generator, and a microbubble, which not only provides energy for the propulsion but also plays a key role for functioning. Due to the embedded ferromagnetic nickel (Ni) layer on the surface of the JM (**Figure 2**a), the orientation and rotation of the microrobot can be modulated by an external magnetic field, which can be controlled remotely using a programmable gamepad. Interestingly, we show a unique mechanism of the remote magnetic control that allows us to speed up the microrobot without increasing "fuel," which has not been reported before. The bubble microrobot uses the combination of hydrodynamic effect from bubble collapse and surface tension to function instead of conventional mechanical means that are based on hinge, gear, arms, etc. Despite the simple structure, various functions, such as cargo directional pushing, cargo capturing, long-range sweeping, and self-anchoring (Figure 1), can be achieved by multiple working modes of the bubble microrobot that simply depend on the relative position between the micromotor and the target cargo. In particular, the switch between different modes can be easily realized by a real-time manipulation using a gamepad. This gamepad control clearly shows the great maneuverability and controllability of our bubble microrobot, which is a substantial progress compared with existing methods. We further unveil the underlying mechanisms of the microbubble–microparticle interactions from near-field hydrodynamic effect to far-field surface capillary wave effect. Our findings demonstrate a substantial advance of the multimodal bubble microrobot specifically working near the air–liquid interface, and depict the nonintuitive mechanisms that offer helpful insights for developing swimming microrobots working in complicated environments.

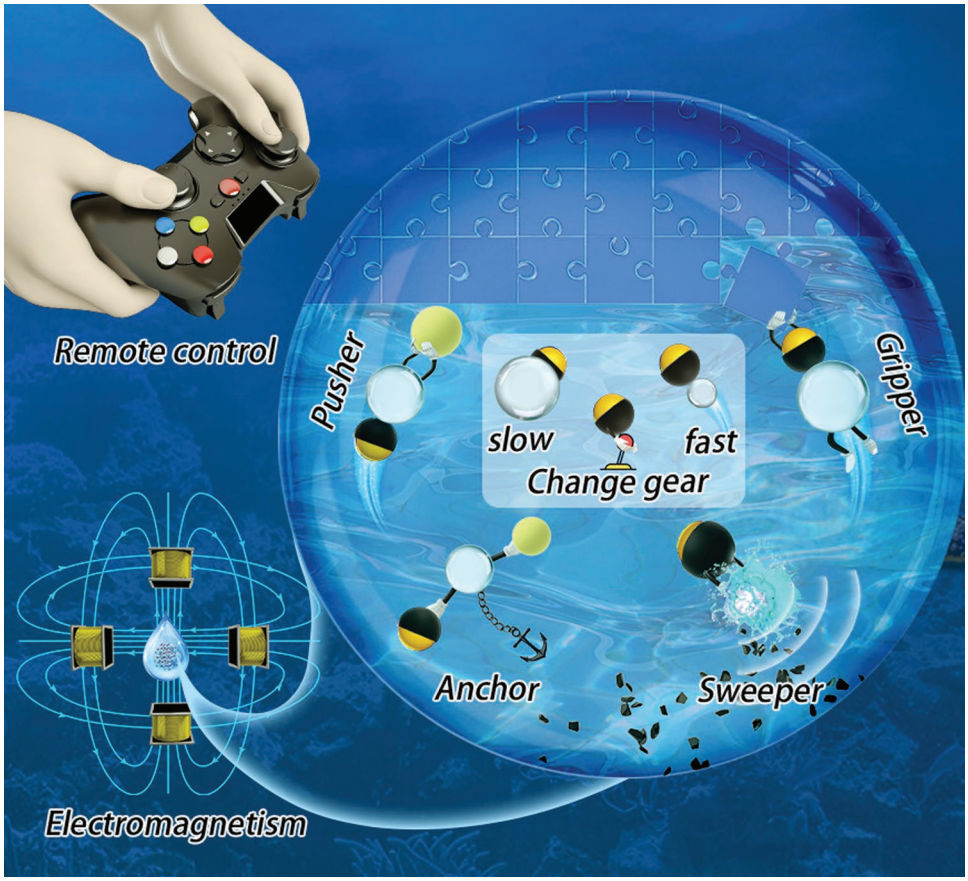

Figure 1. Schematic diagram of the multifunctional bubble microrobot at different working modes near the free air–liquid surface. Various working modes, including gripper, pusher, sweeper, and anchor can be achieved based on different microbubble–microparticle interactions under a programmable magnetic field. Using a simple gamepad, we can not only manipulate the orientation and rotational motion of the bubble microrobot but also remotely change the speed of the microrobot without adding fuel, in a manner similar to "change gear" of driving a vehicle.

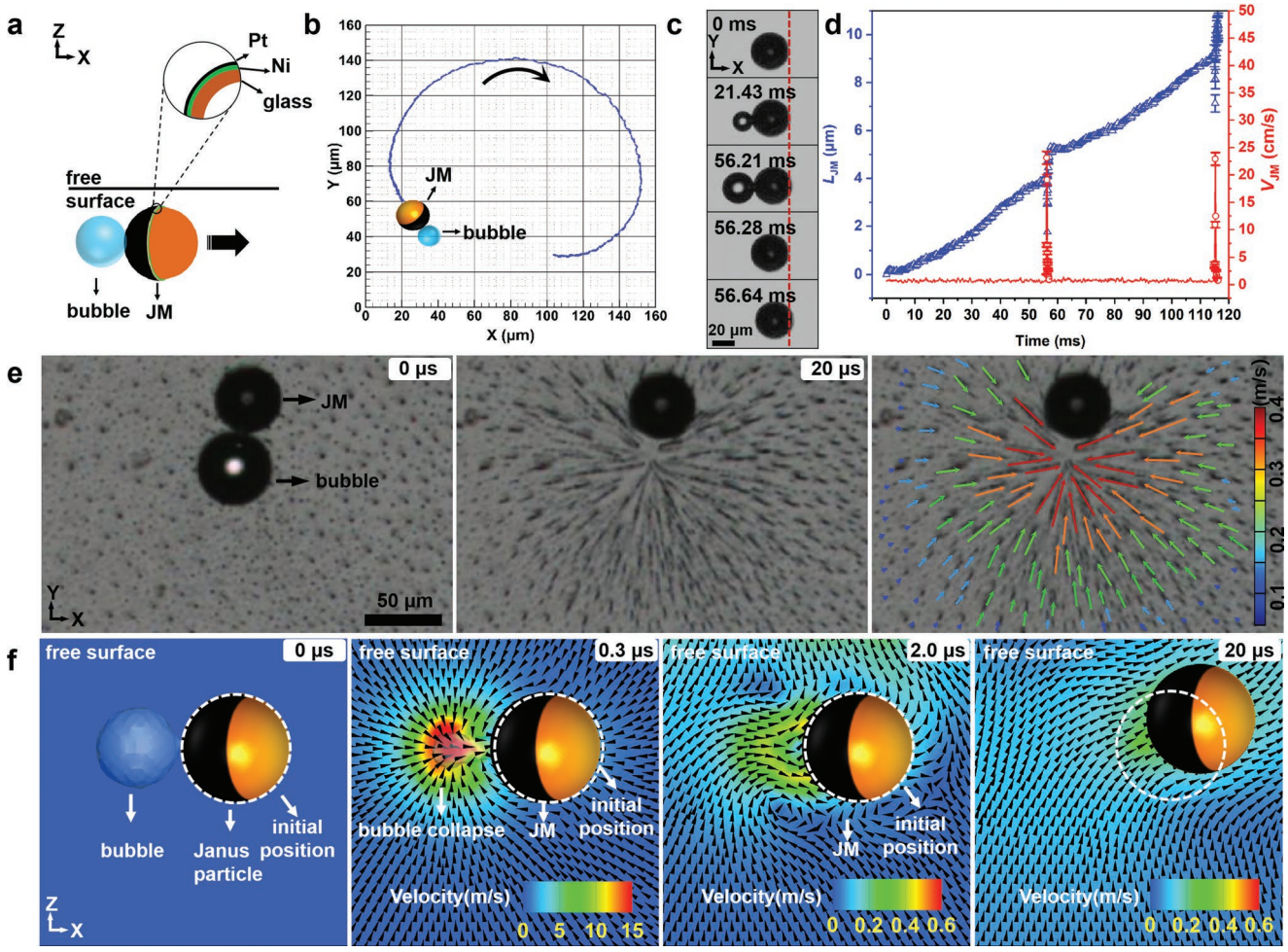

Figure 2. Self-propulsion mechanism of a bubble microrobot. a) Schematic diagram of the JM; the thicknesses of the Ni and Pt layers are 40 and 20 nm respectively. b) A typical trajectory of a bubble microrobot (diameter $d = 39.5 \pm 0.5$ μm) lasting 3.44 s in 3% v/v H_2O_2 solution. c) Snapshots during one bubble cycle captured from Movie S1, Supporting Information. The movie was recorded at 50 000 fps. d) Displacement and velocity of the JM in two consecutive cycles. The errorbars are calculated based on the measurement uncertainty of trajectory tracking, which is about 0.5 μm. e) Transient flow field visualization before (left) and after (middle) microbubble collapse using magnetic nanoparticle chains under uniform magnetic field in 3% v/v H_2O_2 solution. The velocity field from the deformation of the magnetic nanoparticle chains is shown in the right. f) Side view of the flow field of bubble collapse obtained by numerical simulation. The arrows denote the magnitude and direction of the flow field; the background color denotes the magnitude of the velocity; the dotted circle marks the initial position of the JM.

2. Results

2.1. Mechanisms of the Bubble Microrobot

The structure of the JM and the configuration of the bubble micromotor are shown in Figure 2a. The JM was fabricated by covering platinum (Pt) and Ni layers on the hemisphere of a hollow glass microsphere (HGM) with diameter (d) = 10–50 μm (see Experimental Section and Note S1, Supporting Information, for details). The thicknesses of the Ni and Pt layers are ≈40 and 20 nm, respectively. The microbubble generated by the catalytic decomposition reaction of H_2O_2 with concentration of 3–5% (v/v, no surfactant is added) is always located at the Pt-side of the JM ($2H_2O_2 \xrightarrow{Pt} 2H_2O + O_2$), and the microrobot moves toward the glass-side. Figure 2b and Movie S1, Supporting Information, show the typical trajectory of the bubble microrobot. According to our experiments, the bubble frequency is usually from 10 to 25 Hz.

In one bubble period seen in Figure 2c, the bubble experiences two stages: slow growth and fast collapse. The growth stage lasts ≈56.2 ms, close to the complete bubble growth-collapse period about 56.6 ms. The instantaneous bubble collapse occurs in ≈10 μs, which can be described by the Rayleigh collapse time[16] $T_{collapse} = 0.915 R_{bmax} \sqrt{\frac{\rho}{p_0 - p_b}}$, where R_{bmax} is the maximum radius of the microbubble when it collapses, ρ is the fluid density, p_0 is the standard atmospheric pressure, and p_b is the pressure inside the bubble. From the variation of displacement and speed shown in Figure 2d (two consecutive periods), we can estimate that in the bubble growth stage the JM's average speed is only about 50 μm s^{-1}, while during bubble collapse the speed is more than 20 cm s^{-1}. Although there is an instantaneous small withdraw of JM appearing after the bubble collapse, the JM still manifests a large positive displacement in the collapse stage.

We show that the collapse of the microbubble causes a strong hydrodynamic flow, which becomes the main energy source for the microrobot to move and work. The generation of the hydrodynamic jet flow by bubble collapse has been theoretically depicted by cavitation theory.[17] To visualize the transient flow field during microbubble collapse, we used superparamagnetic nanoparticles (Fe_3O_4@SiO_2, with a diameter of 500 nm) as tracers. Different from the traditional Micro-PIV method,[18] the supermagnetic nanoparticles form chains under a uniform vertical magnetic field, and the transient flow field of bubble collapse can be "memorized" by the deformation of the magnetic chains. This visualization method is particularly suitable for the measurement of rapid transient flow and can avoid the impact caused by the Brownian motion of tracer particles. Figure 2e captured from Movie S2, Supporting Information, shows the deformation of the magnetic chains in about 20 µs after the microbubble collapse (bottom view, observed with a high-speed camera at 50 000 fps), indicating the transient hydrodynamic flow following the shrinkage of the bubble. It is worth noting that according to the cavitation theory[17b] the jet flow should point to the rigid boundary nearby. Thus, here we always observe that the strong jet flow points toward the Pt surface of the JM, causing a large displacement of the JM in the bubble collapse stage compared with the growth stage. The last image of Figure 2e shows that the jet flow speed could be up to 0.40 ± 0.02 m s^{-1}, implying a surprisingly large Reynolds number Re (Re is a ratio of inertial force over viscous force) ranging from 10 to 50. Such large Re number breaks the scallop theorem constraint[19] for microswimmers at low Re number regime, and introduces dramatic inertial hydrodynamic effect that was usually neglected.

To better illustrate the hydrodynamic effect of the bubble collapse process, we performed a numerical simulation to unveil the hydrodynamic effect based on the volume of fluid method by solving the Navier–Stokes equations (see Note S2, Supporting Information, for details). The diameters of the JM and the microbubble were 20 and 16 µm, respectively. Bubble collapse occurred due to the breakdown of the pressure balance between the inside and the outside of the bubble. The simulation result of the flow field (side view) around the JM during bubble collapse is shown in Figure 2f. After the bubble collapse (Figure 2f, $t = 0.3$ µs), the fluid nearby first flows to the original center position of the microbubble. Then at $t = 20$ µs, we observe a jet flow pointing to the JM with a velocity ≈0.3 m s^{-1}. Such jet flow produces a net forward displacement of 10.6 µm in 20 µs for the JM. We notice that the jet flow direction is slightly inclined upwards due to the existence of the free air–liquid interface. The simulation result in Figure 2f provides higher temporal resolution of the transient jet flow field, and is in good agreement with the experimental result in Figure 2e. We will demonstrate later how this microbubble-induced jet flow could be used as a "bubble tentacle" to push, grasp, and hold other micro-cargos in the near field.

More importantly, we stress that the rapid collapse of the microbubble can generate a capillary wave at the free surface. We recorded the generation and propagation of the surface wave with a high-speed camera in a frame rate of 460 000 fps. Snapshots (from Movie S3, Supporting Information) after the collapse of the microbubble are shown in **Figure 3**. Such surface capillary wave originates from the water surface protrusion caused by the bubble collapse and its propagation along the air–liquid interface, as illustrated by the inset images

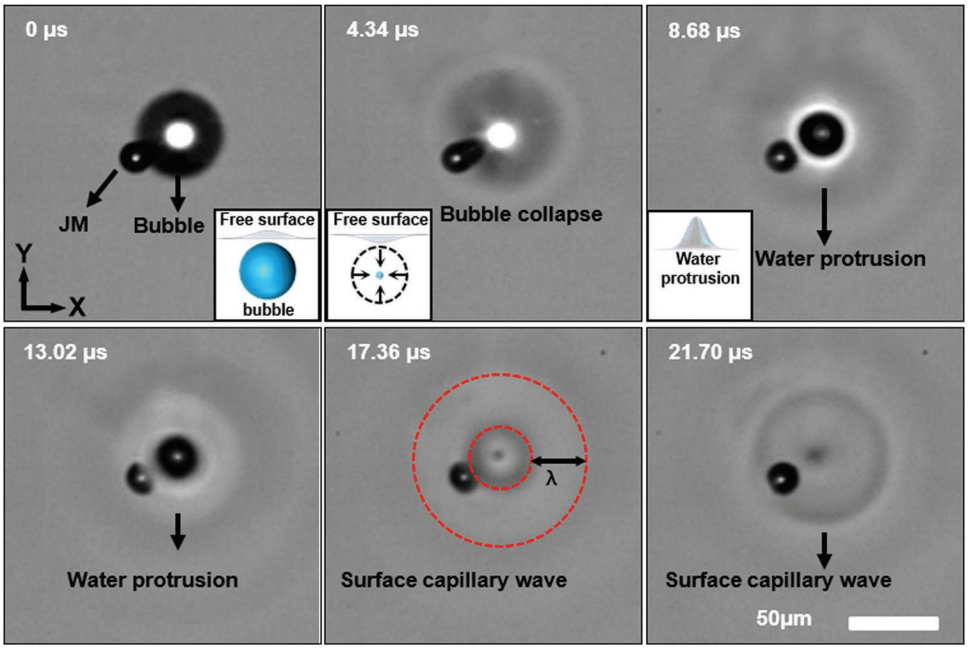

Figure 3. Surface wave generated by microbubble collapse in 5% v/v H_2O_2 solution. We show snapshots obtained by a high-speed camera (460 000 fps, Movie S3, Supporting Information), in which the propagation of the wave can be seen. A diagram of microbubble collapse producing a water protrusion is also provided in the insets (to clearly demonstrate the deformation of the free interface the JM is neglected). The propagation of the surface wave begins following the recovery of the water protrusion. The diameter of the JM, $d = 21.3 \pm 0.5$ µm. The surface capillary wave wavelength λ is measured to be 24.0 ± 1.2 µm, by taking average in $n = 5$ bubble cycles.

in Figure 3. The propagation speed of the surface waves is measured to be ≈4.0 ± 0.2 m s^{-1}, and the wavelength is about 24.0 ± 1.2 µm. According to the capillary wave theory,[20] $v = \sqrt{\frac{2\pi\sigma}{\rho\lambda}}$, where σ is the surface tension coefficient, ρ is the liquid density, and λ is the surface capillary wave wavelength, we find that the theoretical capillary wave velocity is 4.3 m s^{-1}, which is consistent with the wave velocity measured in the experiment. The impact of this surface capillary wave is still noticeable up to almost 500 µm away from the bubble center. We observe that the higher the water protrusion is made, the faster and longer the wave can propagate. Distinct from the microbubble-induced jet flow that exerts impact in the near field, we will show that the surface capillary wave can efficiently manipulate the target microcargos in the far field. Notably, the switch between the near field and far field manipulation can be achieved with the assistance of a vertical magnetic field (see Figure 8f and Movie S13, Supporting Information, and Section 2.3.4 below), which underlines the flexibility and controllability of the bubble microrobot.

2.2. Magnetic Field-Guided Navigation

Although the bubble microrobot moves autonomously, the direction of its motion could be easily affected by the transient flow field induced by the bubble growth and collapse as well as other fluctuations. To achieve deterministic navigation, we fabricated a Ni layer (with a thickness of 40 nm) embedded under the hemispherical Pt layer (with a thickness of 20 nm) on the JM surface, and used a magnetic field to modulate the orientation and rotation of the microrobot. We established a three-axial Helmholtz electromagnetic coil (HEC) system for magnetic actuation (see Experimental Section and Note S3, Supporting Information, for details). Such HEC system produced a uniform magnetic field, whose control signal was programmed on a PC. The strength and direction of the magnetic field could be remotely controlled either by a program or a gamepad connecting to the PC (**Figure 4**a). Due to the fast response of the ferromagnetic Ni layer to the change of the magnetic field direction, the steering of the bubble microrobot was completely under controlled. Interestingly, we found a novel speed modulation method of the bubble microrobot, which turned the microrobot from a slower mode to faster one by switching on the vertical magnetic field without changing the fuel concentration. This easy and switchable speed modulation method demonstrates a substantial progress to improve the maneuverability of the bubble microrobot, which has never been reported before.

2.2.1. Steering of the Bubble Microrobot

The uniform magnetic field from the HEC system does not generate a driving force but only a torque on the Ni layer when

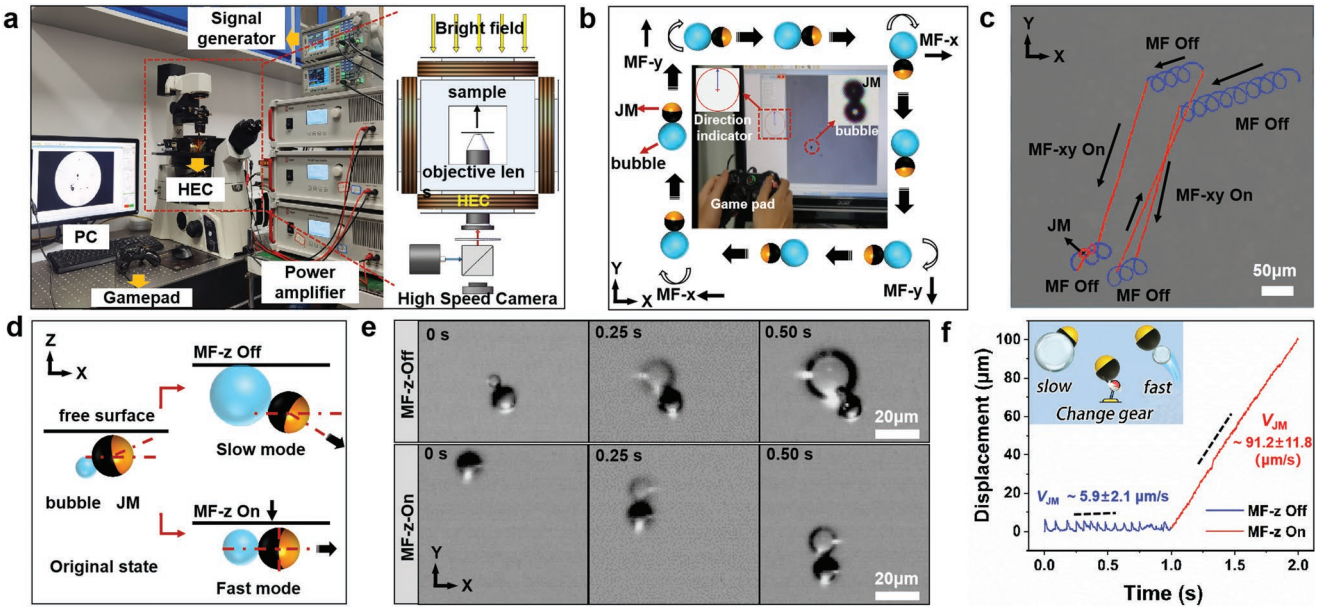

Figure 4. Remote speed modulation and steering of the bubble microrobot guided by a magnetic field. a) 3D magnetic control system based on the HEC. The photo on the left side shows the experimental system used in this work. b) Schematic diagram of the navigation and steering of the bubble microrobot by changing the direction of the uniform magnetic field (MF) in the horizontal *x*–*y* plane. c) Real time trajectory of JM before (MF off, blue circular trajectory) and after (MF-*xy* on, red linear trajectory) applying the horizontal magnetic field. The H_2O_2 concentration is 5% v/v. d) Schematic diagram of the speed modulation of the bubble microrobot by applying a uniform magnetic field in the vertical z plane (MF-*z* on). e) Snapshots from a top view movie (Movie S6, Supporting Information) that manifest the speed-up of the bubble microrobot by applying the vertical *z* magnetic field. From this figure and Movie S6, Supporting Information, one can easily see that the microrobot moves much faster, the microbubble becomes smaller, and the orientation of the JM keeps its horizontal orientation (half bright half dark in the image) when MF-*z* is on. The change of JM's orientation can be observed more clearly in the movie. The H_2O_2 concentration is 5% v/v. f) Speed-up of the bubble microrobot by applying magnetic field in the vertical *z* plane. The average velocity of the bubble microrobot, measured from Movie S6, Supporting Information, increases from about 5.9 ± 2.1 µm s^{-1} in a slow mode when the MF-*z* is off to about 91.2 ± 11.8 µm s^{-1} in a fast mode when the MF-*z* is on. The average speed is calculated using the data of $n = 5$ cycles.

the magnetic dipole moment of the JM is not parallel to the direction of the magnetic field. It is known that the JM obtains a dipole moment and rotates simultaneously with the rotating magnetic field such that its magnetic and nonmagnetic interfaces align with the direction of the field. After aligning with the magnetic field direction, the bubble microrobot will move autonomously along its new orientation. Figure 4b schematically shows the navigation and steering of the bubble microrobot by changing the direction of the uniform magnetic field in the horizontal x–y plane, with the photo in the middle manifesting the real time control of the bubble microrobot (Movie S4, Supporting Information). The remote control of the steering can be done manually by real-time manipulation of a gamepad as shown in Figure 4b, or be achieved by pre-designed program, providing flexible strategies for the reliable real-time control of the bubble microrobot. Figure 4c (Movie S5, Supporting Information) shows the real time trajectory of the JM before and after applying the horizontal uniform magnetic field, which shows the switching from a typical circular motion (blue trajectory) to a linear motion (red trajectory) aligned to the magnetic field. The circular motion without applying a magnetic field was attributed to the asymmetric and nonuniform surface properties of the JM caused by fabrication.[8d] Directed motion is simultaneously formed after applying the magnetic field demonstrating a reliable magnetic field-guided navigation.

2.2.2. Remote Speed Modulation of the Bubble Microrobot

We report a novel and convenient method to remotely control the speed of the bubble microrobot. Different from previous methods that need to change the fuel concentration or establish magnetic field gradient with complicated setup, our method simply adjusts the orientation of the JM by switching on/off the vertical magnetic field.

To better understand the underlying mechanism, Figure 4d gives a schematic diagram showing how the applied vertical magnetic field (MF-z) changes the orientation and propulsion of the JM as well as how the interface confinement influences the bubble size and frequency. When the magnetic field is off, the exact orientation of the JM is slightly upwards from the side view, due to the gravity of the heavier metal side. While applying a vertical magnetic field (referred to as MF-z On in Figure 4d), the orientation of the JM should align with the magnetic field and strictly face the horizontal direction. From the experimental movie (Movie S6, Supporting Information) and the corresponding snapshots (Figure 4e), we clearly observe that the JM's orientation keeps horizontal after applying the vertical magnetic field, that is, from the top view the JM always manifests half bright half dark (bottom row of MF-z On in Figure 4e) compared with the original state showing a larger bright fraction (the first snapshot of the top row of MF-z Off in Figure 4e). At the meantime, the maximum bubble size reduces due to the increased confinement from the air–liquid interface when the JM's orientation keeps horizontal with MF-z On, which also causes bubble generation frequency increases to about 50–100 Hz. The average speed of the bubble microrobot under vertical magnetic field is measured to be $\approx 91.2 \pm 11.8$ μm s^{-1}, which could reach almost ten times larger than the speed when the magnetic field is absent (Figure 4f).

The above phenomena in combination with the illustrations in Figure 4e,f, indicate a remote speed modulation method closely related to the orientation of the JM. However, the underlying mechanism is more complicated as the change of JM's orientation also influences the bubble dynamics and the hydrodynamic jet flow. When the magnetic field is off, the JM's orientation gradually turns downward along with the growth of the bubble. During this process, owing to the much lower density of the bubble, the JM's vertical position also moves down (Figure 4e). As a result, the bubble collapse-induced jet flow is not focused to the horizontal direction. In contrast, when a vertical magnetic field is applied, the strict alignment of the orientation to the magnetic field causes the JM–bubble combination to stay in the same horizontal plane near the air–liquid interface (Figure 4e). This results in two consequences: 1) the jet flow from bubble collapse is more focused to the horizontal direction, that is, providing stronger propulsion in horizontal direction; 2) the confinement of the air–liquid interface restricts the maximum size that the bubble can grow to, and thus increases the bubble frequency. As a result, the hydrodynamic jet impulse exerted on the JM is stronger and more frequent compared with the situation without magnetic field. It is interesting to note that a similar speed enhancement, called tilt rectification,[21] has been recently reported from an electric-photochemical hybrid micromotor near a solid–liquid interface. No matter near an air–liquid interface or a solid–liquid interface, we might adjust the orientation of the micromotor to delicately change the performance by employing the interfacial confinement effect.

Therefore, we can not only remotely manipulate the steering of the bubble microrobot by a horizontal magnetic field but also utilize a vertical magnetic field to speed up the micromotor. This speed modulation method switches the bubble microrobot's navigation from slow mode to fast mode in a simple and programmable way analogous to "change gear" in driving a vehicle, which dramatically improves the maneuverability of the bubble microrobot. Although not shown here, we also found that it is possible to fine tune the speed by varying the inclination angle of the magnetic field via the three-axial HEC system. The range of the average speed under magnetic modulation could be very wide, approximately from 5 to 200 μm s^{-1}.

2.3. Multiple Working Modes of the Bubble Microrobot

Hereafter, we will demonstrate four working modes of the bubble microrobot, that is, pusher, gripper, anchor, and sweeper. The working modes are easily switchable, and depend on several factors including the initial position of the bubble microrobot and the target micro-cargo, the orientation of the JM, and the size ratio between the JM and the target micro-cargo.

2.3.1. Pusher

The bubble microrobot can serve as a "pusher" for cargo delivery when it approaches a microparticle whose diameter is larger

than the JM. To establish the pusher mode, we first used magnetic field to guide the bubble microrobot's motion toward the target microparticle. When the microrobot was approaching the target, we rapidly turned the JM's orientation by adjusting the magnetic field direction to align the microbubble with the target microparticle (see Movie S7, Supporting Information), establishing a JM–bubble–microparticle (J–B–M) configuration. **Figure 5**a shows the experimental trajectory of the target microparticle (top left inset) and the displacements of both bubble microrobot and microparticle in consecutive ten cycles, respectively. With periodic bubble growth and collapse, the bubble microrobot pushes the microparticle with an average velocity more than 100 μm s^{-1}. In each cycle, as shown by the bottom right inset enlarged from the rectangular area in Figure 5a, we observe three stages of the motions for both JM and microparticle. The large microparticle manifests a stepwise displacement of L_P (blue triangles) with an increment of ≈2.4 ± 0.3 μm during the whole cycle lasting 12 ms, while the displacement of JM (L_{JM}) (red circles) varies reciprocally.

To provide more details, we use experimental images (Figure 5b) and schematic diagrams (Figure 5c) to depict the three stages of the pusher mode based on the bubble dynamics and the motions of both JM and microparticle. 1) In the first stage, the microbubble keeps growing while it has not contacted with the microparticle. The JM moves slightly backward accompanying the growth of the microbubble, and the larger microparticle doesn't move forward as the interaction with the microbubble is very weak. 2) The second stage will begin when the microbubble gets in contact with the microparticle. The bubble interacts with both microparticle and JM, and transfers the momentum to them. According to the conservation of momentum, the microparticle moves forward and the JM gains the reverse momentum, resulting in displacements in opposite directions. 3) The third stage corresponds to the microbubble collapse. As the JM's size is smaller than the target microparticle in the pusher mode, the jet flow points to the rigid boundary of the larger microparticle based on the mechanism shown in Figure 2. Under such flow, the microparticle is

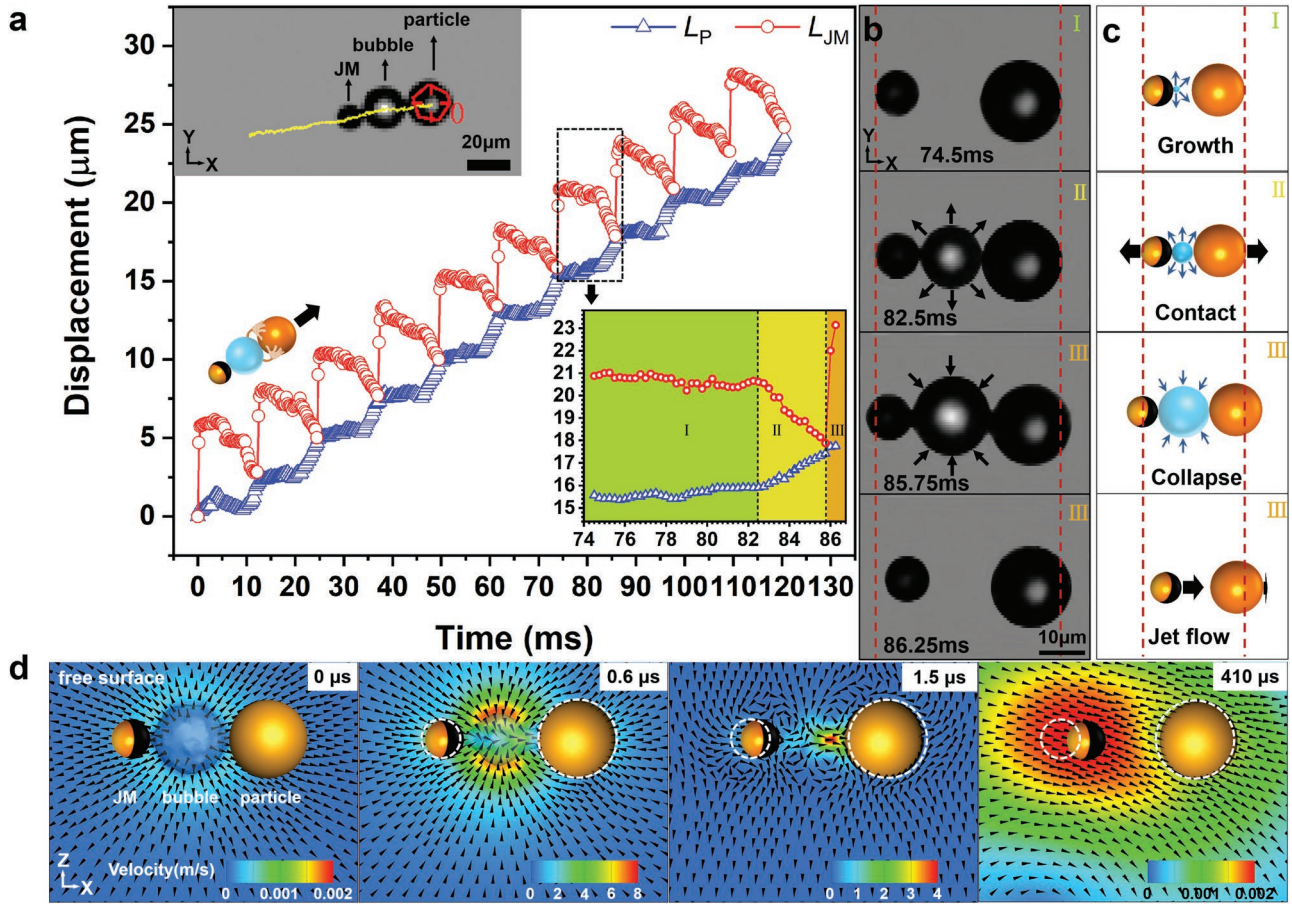

Figure 5. Experimental demonstration and numerical simulation of the pusher mode. a) Displacements of the target microparticle (size 19.4 μm) and the JM (d = 13.0 μm) in n = 10 cycles. The experiment was carried out in 5% v/v H_2O_2 solution. Insets: experimental trajectory of the target microparticle in 0.37 s (top left); displacement of the JM and microparticle in one single cycle (bottom right). b,c) Experimental images and schematic diagram of the motion of the large microparticle pushed by the JM in one single cycle, the red dotted lines mark the initial positions of the JM and microparticle. This cycle corresponds to the one shown in the bottom right inset of (a). d) Numerical simulation of the flow field of the pusher after the bubble collapse. The right side is defined as the positive direction. The diameters of the JM, bubble, and microparticle are 10, 20, and 20 μm, respectively. The arrows denote the magnitude and direction of the flow field; the background color denotes the magnitude of the velocity; the dotted circle marks the initial positions of the JM and microparticle.

propelled forward and the JM moves following the microparticle as well. In a whole cycle, the target microparticle obtain a net positive displacement, and the bubble microrobot's advance can be understood by the ratchet effect[22] (Movie S7, Supporting Information). As a result, the pusher configuration provides an efficient method for a smaller microrobot to propel a larger cargo with a speed more than 100 μm s^{-1}.

We want to highlight that the motions and the displacements of both target microparticle and microrobot in different bubble cycles are highly repeatable, indicating that the pusher configuration is stable and sustainable. To stop the pusher mode, we only need to use the gamepad to rapidly change the orientation of the JM by magnetic manipulation and release the cargo from the pusher. In addition, the pusher configuration of the bubble microrobot can also propel multiple large microparticles or cargos with different shapes, as shown in Movie S8A, Supporting Information. In the experiments, we successfully used the pusher to push a target cargo which is about 500 times heavier than the JM. It is interesting to see from Movie S9A, Supporting Information, that we can flexibly modulate the speed of the pusher even when it is working with a heavy load.

From the above results, we can see that the key mechanism of the pusher mode is the hydrodynamics of microbubble collapse confined by both "soft" air–liquid interface and "hard" liquid-particle boundaries, which hasn't drawn sufficient research attention yet. According to experimental observations, we simulated the flow field and the motions of JM and target microparticle on both sides of the microbubble to better understand the mechanism of the pusher mode. Figure 5d shows the numerical simulation of the flow field of the pusher mode after bubble collapse. The bubble starts to collapse due to the pressure difference between the inside and outside of the bubble, and the surrounding fluid flows toward the bubble cavitation, dragging both JM and microparticle to move closer to each other (0.6 μs). The deformable air–liquid interface influences the direction and the evolution of the jet flow (1.5 μs), which moves away from the free surface and is inclined to the big microparticle on the right. After that, the simulation shows that the flow propels both JM and microparticle to the side of the large microparticle (410 μs), which is consistent with the experimental phenomenon.

2.3.2. Gripper

Although the pusher mode can reach a relatively high propulsion speed, it is difficult for the microrobot to hold and rotate the target cargo in the above J–B–M configuration, as the bubble can hardly transfer a torque to the cargo. To tackle such problem, we establish a "gripper" mode that simply changes the J–B–M configuration to the B–J–M configuration. This B–J–M configuration will be formed as long as the glass side of the JM contact the microparticle, as shown in **Figure 6**a (the microparticle is labeled with pseudo color to distinct from the microrobot) and Movie S10A, Supporting Information. The most intriguing phenomenon is that the microrobot can firmly "grasp" the micro-cargo in the front region of the glass hemisphere of the JM (Figure 6a), which can be explained by the "Cheerios effect."[23] The Cheerios effect originates from the phenomenon that floating objects appear to either attract or repel one another. It is necessary to stress that the Cheerios effect near the air–liquid interface strongly relies on the surface wetting properties of the JM and the microparticle. If their surfaces are both hydrophilic and hydrophobic, the fluid pressure in the region between the objects is lower than the pressure outside, due to the larger capillary pressure drop across the meniscus with smaller curvature radius. As the JM is hydrophilic, it can grip any hydrophilic microparticles when approaching them due to the low fluid pressure between the JM and the target microparticles.

Once the micro-cargo is gripped by the microrobot, reliable delivery will be done with the assistance of the magnetic field. We show in Figure 6b that the bubble microrobot together with the gripped microparticle rotates under a spinning magnetic field (also see Movie S10B, Supporting Information). The microparticle keeps attaching with the JM firmly even when the rotational speed is up to ≈100 rpm. To release the microparticle, we can suddenly change the orientation of the JM by applying a transient rotation magnetic field, as shown in the last image of Figure 6a. Furthermore, the microrobot gripper can catch more than one microparticle at the same time. Figure 6c shows that the microrobot captures microparticles one by one under our control (Movie S10C, Supporting Information). And Figure 6d displays that even having gripped a cluster of microparticles, the microrobot can change direction and perform delivery easily (Movie S10D, Supporting Information).

It is necessary to emphasize the difference between the gripper and the pusher, as seemingly they both push targets. Note that it is difficult to use bubble's surface to continuously exert grasping effect, as bubble will periodically disappear and using its interface to grasp target is not firm. Thanks to the Cheerios effect explained above, the bubble gripper can grasp one particle or a cluster of particles and rotate freely (Movie S10, Supporting Information). In addition, the gripper can grasp the target not only using the front part (Movie S10A, Supporting Information) of the JM but also the side part (Movie S10B, Supporting Information). These features are unique for gripper and cannot be done by a pusher. The combination of the gripper and pusher modes that are easily switchable could widen the application of the bubble microrobot.

Figure 6e provides a schematic diagram for the whole process from capturing the microparticle to releasing it. The results of the gripper mode demonstrate the high maneuverability of the bubble microrobot. Additionally, we find that the translational speed of the gripper mode with a target cargo about 500 times heavier than the JM is ≈5.1 ± 0.2 μm s^{-1}, about 30% less than the pusher mode, as shown in Figure 6f and Movie S8, Supporting Information. Similarly, the speed of the gripper can be remotely modulated during working, as shown in Movie S9B, Supporting Information.

2.3.3. Anchor

We have shown that in the pusher mode the hydrodynamic jet flow inclines to propel the particle with larger size was used as the source of the propulsion. Naturally, one would ask what will happen when the microparticle is equivalent to the JM. In such

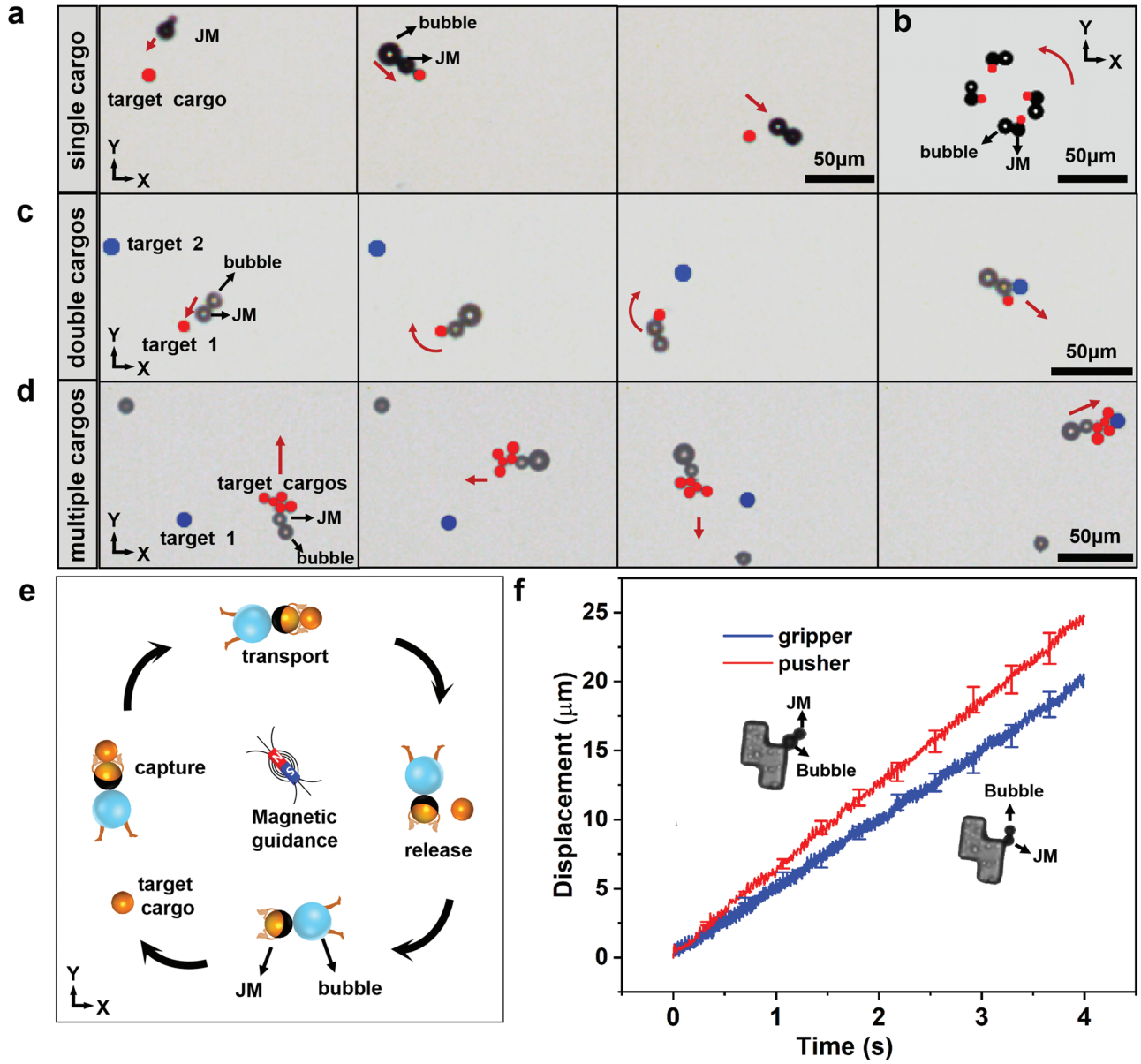

Figure 6. Bubble microrobot serves as gripper for delivery of target microparticles. a) The gripper grasps and releases a single target microparticle (Movie S10A, Supporting Information). b) The gripper can firmly catch the microparticle and stably rotate under a spinning magnetic field (0.1 Hz, Movie S10B, Supporting Information). c) The gripper captures two microparticles one by one (Movie S10C, Supporting Information), and d) catches a cluster of microparticles (Movie S10D, Supporting Information). To facilitate the distinction between JM and microparticles, we mark the microparticles with pseudo color (red and blue). The red arrows denote the moving direction of the bubble microrobot. e) A schematic diagram summarizes how the gripper works. f) A comparison between the delivery of a large and heavy "Z" like Tetris in gripper and pusher two modes (Movie S8, Supporting Information). Errorbars are marked to display the measurement uncertainty from tracking. All the experiments in this figure were carried out in 5% v/v H_2O_2 solution.

a symmetric system, the hydrodynamic effect should be symmetric as well and the flow points vertically downwards, manifesting no preferential direction on either side. Thus, we can employ this symmetric hydrodynamic effect to trap surrounding JM and microparticles based on a new "anchor" mode.

We demonstrate the symmetric JM–bubble–microparticle (sJ–B–M) configuration of the anchor mode in **Figure 7** and Movie S11, Supporting Information. The process in one single bubble growth-collapse cycle is similar to that in pusher configuration (Figure 5b,c), except that the motions of both target microparticle and JM caused by bubble growth and jet flow are always symmetric. Figure 7a illustrates that both microparticle and JM obtain no net displacement but manifests reciprocal motion in four cycles. We find that, as shown in Figure 7b,c, the microparticle and JM are repelled from the microbubble during bubble growth stage and they are dragged toward the bubble cavitation by the surrounding hydrodynamic flow during bubble collapse stage. Such reciprocal motion

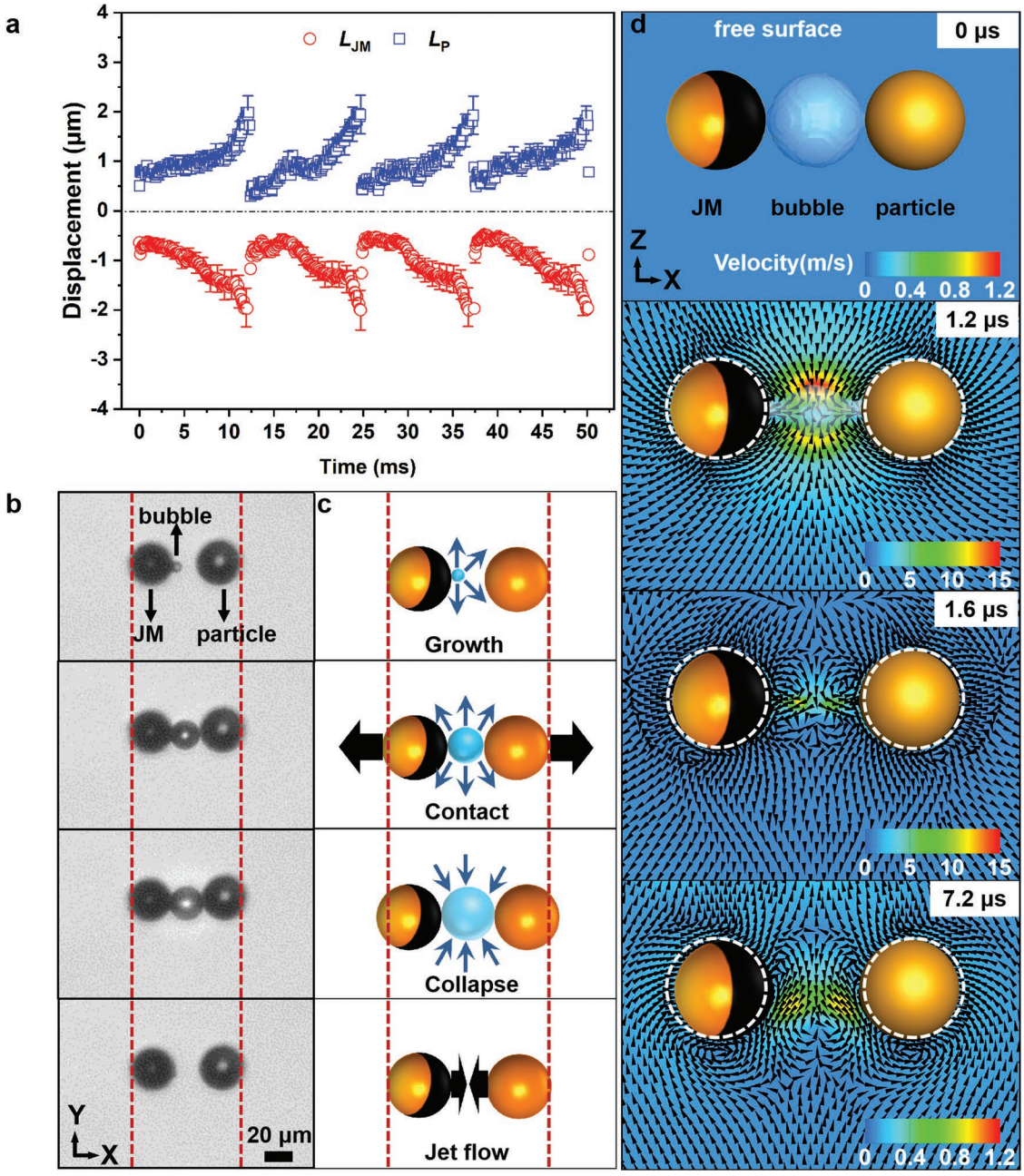

Figure 7. Experiments and numerical simulation of the anchor configuration. a) The displacements of the JM and microparticle in four bubble cycles in 5% v/v H_2O_2 solution. Errorbars are marked to display the measurement uncertainty from tracking. b,c) Experimental images and schematic diagram of the anchor mode in a single bubble cycle, the red dotted lines mark the initial positions of the JM and microparticle. d) Numerical simulation of the flow field of the anchor mode after bubble collapse. The arrows denote the magnitude and direction of the flow field; the background color denotes the magnitude of the velocity; the dotted circle marks the initial positions of the JM and microparticle.

doesn't produce any net displacement by anchoring target microparticle to the bubble microrobot.

We also perform numerical simulation to illustrate the detail of the hydrodynamic flow and particle motions during bubble collapse, as shown in Figure 7d. The JM and microparticle reveal the same magnitude of displacement and velocity but in opposite directions (Figure 7d), which is in agreement with the experimental observation. The simulation verifies that the hydrodynamic flow caused by the bubble collapse is always symmetric and points vertically downwards (7.2 μs in Figure 7d). We stress that, once this anchor configuration is established, the target microparticle will be anchored to the bubble micromotor for a long time without any assistance of the magnetic field. Again, to release the microparticle, we can apply a magnetic field to break the sJ–B–M configuration, such as a sudden rotation of the JM using spinning magnetic field.

2.3.4. Sweeper

The presence of the free air–liquid interface offers an alternative approach to deal with far field microparticles using surface capillary wave. The collapse of the microbubble at the air–liquid interface induces not only a jet flow but also a surface capillary wave propagating along the interface. Compared with the near-field interaction mentioned above, the surface capillary wave acting on the microparticles from the far field can extend the working distance of the bubble microrobot remarkably. **Figure 8**a,b (see Movie S12A,B, Supporting Information) shows two examples of this far-field "sweeper" using the surface capillary wave to sweep microparticles faraway. From a bottom view shown in Figure 8a, the propagation of the surface wave is about 4.0 m s^{-1}, and the surface wave only takes 10 μs to impact the target microparticle (d_p = 8.2 ± 0.3 μm) located about 43.5 μm away from the bubble microrobot. Figure 8b further shows another example in which the surface wave can be used to push a target microparticle (d_p = 15.7 ± 0.3 μm) larger than the JM.

How the surface capillary wave impacts a target microparticle embedded in or floating upon the air–liquid interface is a complicated and nonintuitive issue.[24] In the cases shown in Figure 8a,b, one might notice the slight withdraw of the microparticle at 40 μs after the propagation of the surface wave, indicating a back-and-forth movement caused by the vibration of the soft interface. In Figure 8c,d, we measure the displacement and the velocity of the above two microparticles. We observe that the smaller microparticle manifests a strong forward propulsion with a positive displacement of 1.0 ± 0.1 μm when the front of the first wave reaches it at about 30 μs. But soon after the pass of the first wave (at about 40 μs), the microparticle withdraws ≈0.3 ± 0.1 μm. This back-and-forth movement can be understood as: the interfacial tension exerted on the particle embedded in the interface will push the particle forward when the particle is located on the front of the wave, and will drag the particle backward when the particle is on the back side of the wave. In one wave period, the particle manifests a net forward displacement as it obtains kinetic energy from the wave propagation. After the arrival of the subsequent waves, the microparticle will be continuously propelled showing an average speed of 0.1 mm s^{-1}. The larger target microparticle shows the similar phenomenon of propulsion by surface capillary wave. The larger particle shows a less positive displacement and more withdraws compared with the smaller microparticle, because it obtains smaller acceleration from the inertial impact caused by the wave. Nonetheless, the measured velocities in both cases (Figure 8d) manifest no clear difference.

Furthermore, such surface wave is efficient to deal with a large number of microparticles at the same time, as shown by Figure 8e (Movie S12C, Supporting Information) in which the sweeper is used to sweep the water surface covered by many floating particles. We have found a method to successfully switch the working modes between near field and far field effect based on the aforementioned mechanism of the speed modulation by vertical magnetic field (Figure 8f and Movie S13, Supporting Information). At the beginning of Movie S13, Supporting Information, we only applied horizontal magnetic field to guide the navigation of the far field sweeper, which can propel the microparticles about 50 μm away from the sweeper. At about 6.5 s of Movie S13, Supporting Information, the far field sweeper mode is switched to a near field mode by applying a vertical magnetic field, after which the microbubble becomes smaller. When the switch is done, the bubble microrobot can move very close to the microparticles without pushing them away by the surface wave. Our ongoing efforts is devoted to combining the far field and near field impacts from the bubble cavitation for more complicated manipulation at the air–liquid interface, such as assembly or construction of functional micro structures.[10b,25]

2.4. Discussions

Developing novel and reliable strategy for remotely control speed of various micromotors or microrobots is urgently needed. We notice that lately there have been a few results of other morphologies or types of micromotors. Tubular micromotor is another morphology of bubble-based micromotor, and a recent experiment showed that magnetic field guidance of the tubular micromotors near air–liquid interface can be enhanced by 34%.[8c] Such speed enhancement was attributed to the increase in the capillary force exerted by the generated bubbles and the regulation of flow regime to laminar through the tubular micromotor. Comparing with the tubular micromotors, our method for spherical micromotors relies on focusing on the bubble collapse-induced jet flow to the JM and increasing the jet frequency by the assistance from the air–liquid interface and the magnetic guidance.

Intriguing speed control methods have been reported near solid–liquid interface as well. As mentioned above, Xiao et al. showed a novel technique of tilt rectification,[21] which could be used to smartly control speed of their electric-photochemical hybrid micromotor. The mechanism is closely related to the confinement of the solid wall, which hinders the chemical reaction and causes tilting-induced retardation. Another result near the solid–liquid interface is shown in ref. [5], in which an acoustically powered bubble-based microswimmer capable of autonomous motion in three dimensions was developed. In a megahertz acoustic field, the microswimmer was subject to two predominant forces: the secondary Bjerknes force and a locally generated acoustic streaming propulsive force. The motion perpendicular to the solid wall was modulated by the secondary Bjerknes force, resulting in swimming away from or attachment to the solid boundary. These results are inspiring as they share the similarity of using interface confinement to control speed. Although the mechanisms of their works are not the same as ours, the methods near a solid–liquid interface and our method applied to air–liquid interface might suggest a viable strategy to remotely speed control for various chemically powered microrobots, by using the interface confinement and manipulating the orientation of the micromotor.

It is then natural to ask whether our control method can be extended to other environments rather than air–liquid interface. Generally, our control method needs the air–liquid interface and the buoyancy to restrict the combination of the JM, the bubble, and the target staying almost in a horizontal plane near the interface. Such method is very difficult to apply

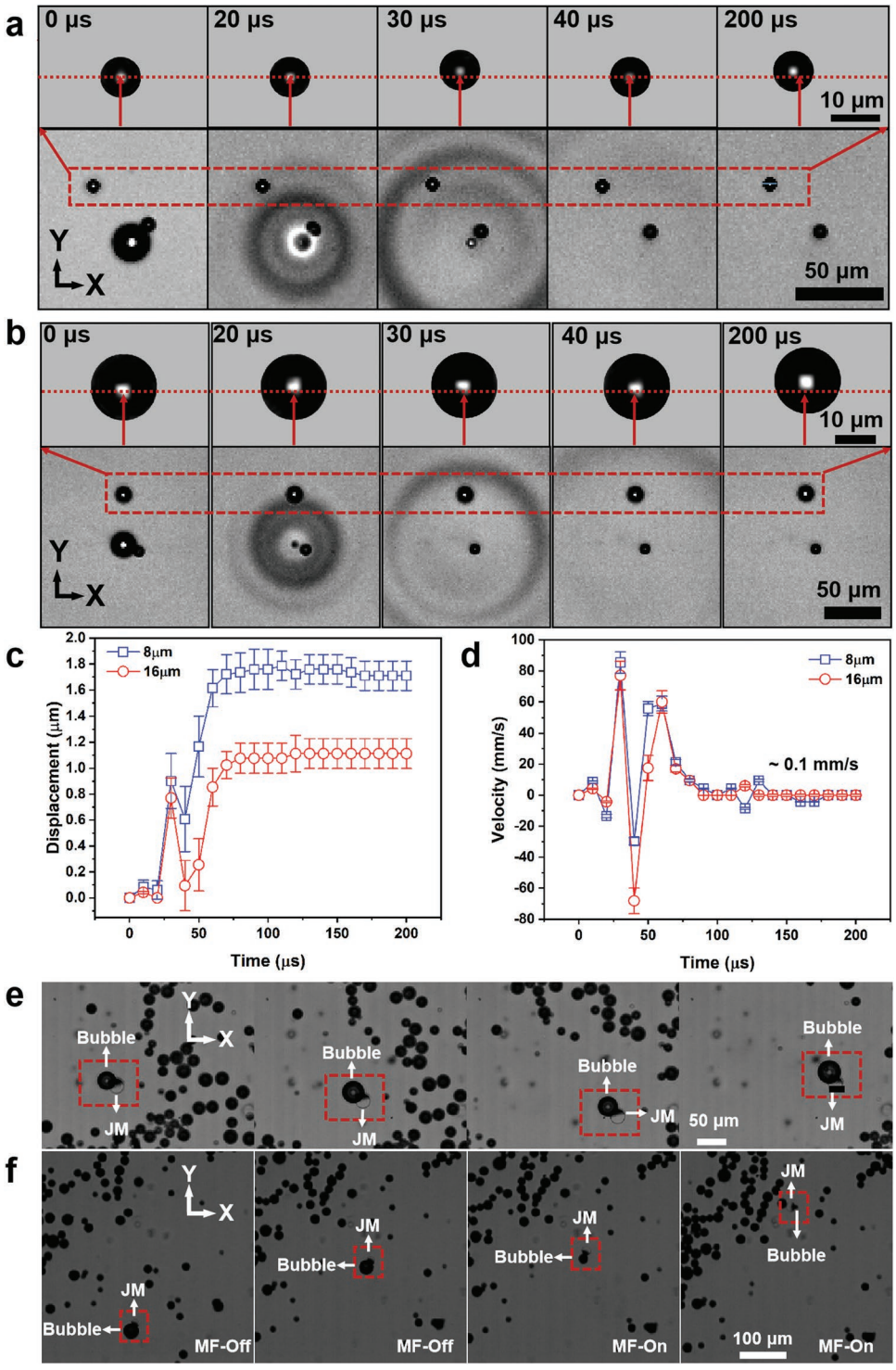

Figure 8. Far field sweeper based on surface capillary wave. a,b) Consecutive snapshots are shown to demonstrate how the surface capillary wave can propel a smaller (a, $d_p = 8.2 \pm 0.3$ μm) and a larger (b, $d_p = 15.7 \pm 0.3$ μm) target microparticles faraway. c,d) Displacement and velocity of the target microparticles shown in (a) and (b) impacted by the surface wave. The errorbars for displacement and velocity are calculated on the basis of standard deviations from $n = 5$ cycles. e) Using sweeper to rapidly sweep a cluster of floating microparticles. f) Switch from a far field (MF-z Off) working mode to a near field one (MF-z On), captured from Movie S13, Supporting Information. The H_2O_2 concentrations here are always 5% v/v.

in the bulk, as buoyancy effect can easily break the combination due to the large density difference between the bubble and solid particles. However, near a liquid–solid interface, if magnetic field is applied to keep the orientation of a heavy micromotor parallel to the solid surface, the impacts of the bubble recoil and collapse might still be used to manipulate nearby particles.

Another interesting issue is the replacement of Pt and Ni by other materials. The present mechanism can be adopted in other solutions where bubble can be generated through other reactions,[26] and using other magnetic materials like Fe_3O_4.[11] In particular, we notice that MnO_2 has been proposed as a good catalyst that can be used to replace expensive Pt,[27] which could significantly reduce the fabrication cost.

3. Conclusions

In conclusion, we show a multimodal bubble microrobot that is specifically designed to work at the air–liquid interface based on magnetic field assisted control. The essential mechanism for manipulating the bubble microrobot depends on the control of the bubble collapse and the induced jet flow with the assistance of the air–liquid interface. This bubble microrobot manifests high controllability and great maneuverability: easy control either by a gamepad or a program, novel method for remote speed modulation by utilizing vertical magnetic field without changing the fuel concentration, convenient switch among different working modes, manipulation for single or multiple targets, and controllable near field and far field impacts. The remote speed modulation relies on the control of the orientation of the JM by the vertical magnetic field, and the manipulation of the direction of the bubble-induced jet flow assisted by the air–liquid interface. We report reliable performances of using the bubble microrobot as pusher, gripper, anchor, and sweeper for micromanipulation of targeted microcargos. The establishment of different working modes depends on adjusting the relative positions among the JM, the bubble and the target, which can be easily realized by the assistance of the gamepad control. Our findings demonstrate a substantial advance of the bubble microrobot working at the air–liquid interface, and depict the nonintuitive mechanisms, including hydrodynamic flow caused by microbubble collapse and mass transfer confined by a free surface, which could serve as effective means for microrobot functioning.

In the emerging applications of microfabrication platform on air–liquid interface and the microtools for surgery,[3c,d,28] the demand of versatile, robust, and multifunction swimming microrobot that can work as microtweezer, microforceps, and microactuator is rapidly growing. The multimodal bubble microrobot shown in this work demonstrates a substantial advance of the swimming microrobot working at the air–liquid interface. The remote speed modulation method significantly promotes the maneuverability and controllability compared with the latest magnetic navigation microrobot.[3b] We do not satisfy with achieving simple function like propelling or capturing only, but integrate different working modes together and make them easily switchable, which can closely meet the demand for working in more complicated situations. The flexible switch between slow speed and fast speed, as well as between near field manipulation and far field effect, is based on the control of the microbubble collapse-induced hydrodynamic jet flow, which is an important and strong effect to overcome the unwelcome influence of surface tension and interfacial disturbance. Such findings offer helpful insights for developing more adaptive swimming microrobots working in complicated environments. For instance, our technique can be used to realize controlled transport of microchips for the emerging microfabrication platform, or controlled clean-up of interfacial pollutants. Our ongoing effort is also devoted to developing a similar multimodal bubble microrobot made of biocompatible materials for cell selecting and fusion in a shallow solution.

The current experimental demonstration of how our multimodal bubble microrobot works relies on the chemical reaction in H_2O_2 solutions. Nonetheless, the mechanism can be adopted in many other solutions where bubble can be generated through other reactions. Thus, even in human body the manipulation method might be utilized in acid environment like stomach[26,29] for drug delivery. The control precision of this multimodal bubble microrobot, up to 10 μm, needs to be improved, which is mainly due to the delayed response of our magnetic manipulation system. Furthermore, scaling up of the multimodal bubble microrobot and collective control of many such microrobots still encounter many problems. For instance, it is a big challenge to separately manipulate different microrobots under the same uniform magnetic field. Coordination with a large number of bubble microrobots that utilize different working modes to complete their individual task is expected to play an important role.

4. Experimental Section

Fabrication of Janus Microrobots: The hollow magnetic Janus micromotors were fabricated by coating Ni (≈40 nm) and Pt (≈20 nm) layers successively on the hemispheres of HGMs. The fabrication procedure is shown in Figure S1, Supporting Information. The HGMs (diameter: 10–50 μm, GS60, density: 600 kg m^{-3}) were purchased from Sino-steel Co. Ltd, and main component was SiO_2. HGMs of different particle size distribution could be obtained through screening and floatation. During fabrication, the dilute solution of the HGMs (10–50 μm) was uniformly spread on a hydrophilic polished silicon wafer and dried at 60 °C to form a monolayer of HGMs on the silicon wafer. Then, a Ni layer with thickness of ≈40 nm and a Pt layer with thickness of ≈20 nm were successively evaporated on the surface of HGMs using an electron beam evaporator. Due to the compact arrangement of the HGMs, the Ni and Pt layers only covered the top hemispheres of the HGMs. The SEM and energy dispersive X-ray images in Figure S1, Supporting Information, clearly show the Janus structure. The density of JM was lower than that of water, so that the JM could move near the air–liquid interface.

Magnetic Manipulation System: A system was established for magnetic actuation. The magnetic field setup consisted of a computer, a gamepad, two signal generator, three power amplifier, and a set of three-axial HEC equipped on the inverted optical microscope (Nikon Eclipse Ti-U) (see Figure 4a). The output signal from the signal generator was amplified by the power amplifier. The amplified signal was used to drive a set of HEC, which generated a uniform magnetic field in arbitrary direction. Herein, the flexible adjustment of magnetic field direction was achieved through a gamepad with various self-defined programmed functions, and the signal generator was controlled by the gamepad to generate predetermined signals. The programming language was C++, the controller programming interface was Windows Multimedia Joystick API, and the serial port (RS-232 standard interface) programming interface was based on System. IO. Ports were provided by NET Framework 4.0. More details can be found in Note S3, Supporting Information.

Experimental Observation and Analysis: The self-propulsion of the Janus microrobot was observed under an inverted microscope (Olympus IX71) equipped with a high-speed camera (Phantom v2512). The HEC system was equipped at the microscope platform to provide a 3D magnetic field for the control of the microrobot. The objective lens was

×10 or ×20, and the frame frequency of the high-speed camera was up to 460 000 fps. Sometimes, to better visualize the half bright half dark state of the JM, a stereomicroscope was used to record image from the top view (such as Figure 4e). The concentration of H_2O_2 was approximately from 3 – 5% v/v. The experimental movies were analyzed with Movie Spot Tracker and ImageJ. In order to analyze the motion of the JM and reveal the mechanism, the flow field of microbubble collapse process was visualized using superparamagnetic nanoparticles (Fe_3O_4@SiO_2, diameter 500 nm) as tracers.

Statistical Analysis: Results were expressed as mean ± standard deviation in all experiments, except for the tracking of one micromotor in Figures 2d and 7a, where the errorbars were calculated based on the half-pixel uncertainty of determining micromotor's movement from image, which was about 0.5 µm. All the displacements and velocities were obtained by analyzing the experimental movies with Video Spot Tracker v08.01.02 with a precision of 0.5 pixel. Sample size in each analysis was usually $n = 5$, as mentioned in figure captions. Statistical computations were made with Matlab, and graphs were made with Origin software.

Supporting Information

Supporting Information is available from the Wiley Online Library or from the author.

Acknowledgements

Le.W. and L.C. contributed equally to this work. The authors thank Prof. Wei Wang from HITSZ for fruitful discussion. The authors are grateful to Prof. Yanpeng Wei and Dr. Yacong Guo from Institute of Mechanics, CAS for the assistance of experiment using high-speed camera. The research work was financially supported by National Natural Science Foundation of China (Grant Nos. 12072350, 11972351, and 11832017), Chinese Academy of Sciences Key Research Program of Frontier Sciences (QYZDBSSW-JSC036), Strategic Priority Research Program of Chinese Academy of Sciences (XDB22040403), Key Research and Development Program of Shaanxi Province (2021ZDLSF05-04), and Natural Science Basic Research Plan in Shaanxi Province (2020JM-479).

Conflict of Interest

The authors declare no conflict of interest.

Data Availability Statement

The data that support the findings of this study are available from the corresponding author upon reasonable request.

Keywords

air–liquid interfaces, bubble microrobots, magnetic actuation, multiple working modes, remote speed control

Received: June 22, 2022
Revised: August 9, 2022
Published online: August 31, 2022

[1] a) J. J. Abbott, E. Diller, A. J. Petruska, *Annu. Rev. Control Rob. Auton. Syst.* **2020**, *3*, 57; b) B. Dai, J. Wang, Z. Xiong, X. Zhan, W. Dai, C. C. Li, S. P. Feng, J. Tang, *Nat. Nanotechnol.* **2016**, *11*, 1087; c) W. Wang, W. T. Duan, S. Ahmed, T. E. Mallouk, A. Sen, *Nano Today* **2013**, *8*, 531; d) K. Zhang, Y. Ren, M. Zhao, T. Jiang, L. Hou, H. Jiang, *Anal. Chem.* **2021**, *93*, 2560; e) Y. Yu, J. Guo, M. Zou, L. Cai, Y. Zhao, *Chem. - Asian J.* **2019**, *14*, 2417; f) B. Mazzolai, F. Carpi, K. Suzumori, M. Cianchetti, T. Speck, S. K. Smoukov, I. Burgert, T. Keplinger, G. Siqueira, F. Vanneste, O. Goury, C. Duriez, T. Nanayakkara, B. Vanderborght, J. Brancart, S. Terryn, S. Rich, R. Liu, K. Fukuda, T. Someya, M. Calisti, C. Laschi, W. Sun, G. Wang, L. Wen, R. Baines, S. K. Patiballa, R. Kramer, D. Rus, P. Fischer, et al., *Multifunct. Mater.* **2022**, https://doi.org/10.1088/2399-7532/ac4c95; g) P. E. Dupont, B. J. Nelson, M. Goldfarb, B. Hannaford, A. Menciassi, M. K. O'Malley, N. Simaan, P. Valdastri, G. Z. Yang, *Sci. Rob.* **2021**, *6*, eabi8017; h) W. E. Uspal, M. N. Popescu, S. Dietrich, M. Tasinkevych, *Soft Matter* **2015**, *11*, 434.

[2] a) A. Purushothaman, S. P. Thampi, *Soft Matter* **2021**, *17*, 3380; b) Z. Y. Xiao, M. S. Wei, W. Wang, *ACS Appl. Mater. Interfaces* **2019**, *11*, 6667; c) C. R. Chen, E. Karshalev, J. G. Guan, J. Wang, *Small* **2018**, *14*, 1704252.

[3] a) J. Li, B. E.-F. de Ávila, W. Gao, L. Zhang, J. Wang, *Sci. Rob.* **2017**, *2*, eaam6431; b) B. Wang, K. F. Chan, K. Yuan, Q. Q. Wang, X. F. Xia, L. D. Yang, H. Ko, Y. X. J. Wang, J. J. Y. Sung, P. W. Y. Chiu, L. Zhang, *Sci. Rob.* **2021**, *6*, eabd2813; c) I. C. Yasa, H. Ceylan, U. Bozuyuk, A. M. Wild, M. Sitti, *Sci. Rob.* **2020**, *5*, eaaz3867; d) K. T. Nguyen, G. J. Go, Z. Jin, B. A. Darmawan, A. Yoo, S. Kim, M. H. Nan, S. B. Lee, B. Kang, C. S. Kim, H. Li, D. Bang, J. O. Park, E. Choi, *Adv. Healthcare Mater.* **2021**, *10*, 2001681; e) J. Llacer-Wintle, A. Rivas-Dapena, X. Z. Chen, E. Pellicer, B. J. Nelson, J. Puigmarti-Luis, S. Pane, *Adv. Mater.* **2021**, *33*, 2102049; f) S. Tang, F. Zhang, H. Gong, F. Wei, J. Zhuang, E. Karshalev, B. E.-F. de Ávila, C. Huang, Z. Zhou, Z. Li, L. Yin, H. Dong, R. H. Fang, X. Zhang, L. Zhang, J. Wang, *Sci. Rob.* **2020**, *5*, aba6137; g) M. Luo, Y. Z. Feng, T. W. Wang, J. G. Guan, *Adv. Funct. Mater.* **2018**, *28*, 1706100.

[4] a) J. Y. Li, X. J. Li, T. Luo, R. Wang, C. C. Liu, S. X. Chen, D. F. Li, J. B. Yue, S. H. Cheng, D. Sun, *Sci. Rob.* **2018**, *3*, eaat8829; b) Y. Ding, F. Qiu, I. S. X. Casadevall, F. W. Y. Chiu, B. J. Nelson, A. de Mello, *Micromachines* **2016**, *7*, 25.

[5] L. Q. Ren, N. Nama, J. M. McNeill, F. Soto, Z. F. Yan, W. Liu, W. Wang, J. Wang, T. E. Mallouk, *Sci. Adv.* **2019**, *5*, eaax3084.

[6] a) P. Suresh, A. F. Long, S. Dumont, *eLife* **2020**, *9*, e53807; b) J. P. Desai, A. Pillarisetti, A. D. Brooks, *Annu. Rev. Biomed. Eng.* **2007**, *9*, 35.

[7] a) T. Li, X. Chang, Z. Wu, J. Li, G. Shao, X. Deng, J. Qiu, B. Guo, G. Zhang, Q. He, L. Li, J. Wang, *ACS Nano* **2017**, *11*, 9268; b) T. Li, A. Zhang, G. Shao, M. Wei, B. Guo, G. Zhang, L. Li, W. Wang, *Adv. Funct. Mater.* **2018**, *28*, 1706066; c) U. Bozuyuk, Y. Alapan, A. Aghakhani, M. Yunusa, M. Sitti, *Proc. Natl. Acad. Sci. USA* **2021**, *118*, e2022090118.

[8] a) A. Barbot, H. J. Tan, M. Power, F. Seichepine, G. Z. Yang, *Sci. Rob.* **2019**, *4*, eaax8336; b) G. Grosjean, M. Hubert, Y. Collard, S. Pillitteri, N. Vandewalle, *Eur. Phys. J. E: Soft Matter Biol. Phys.* **2018**, *41*, 137; c) V. de la Asunción-Nadal, B. Jurado-Sánchez, L. Vázquez, A. Escarpa, *Chem. - Eur. J.* **2019**, *25*, 13157; d) X. Wang, M. In, C. Blanc, A. Würger, M. Nobili, A. Stocco, *Langmuir* **2017**, *33*, 13766.

[9] a) X. Wang, M. In, C. Blanc, M. Nobili, A. Stocco, *Soft Matter* **2015**, *11*, 7376; b) S. T. Chang, V. N. Paunov, D. N. Petsev, O. D. Velev, *Nat. Mater.* **2007**, *6*, 235; c) N. Mano, A. Heller, *J. Am. Chem. Soc.* **2005**, *127*, 11574.

[10] a) J. H. Li, M. Pumera, *Chem. Soc. Rev.* **2021**, *50*, 2794; b) F. N. P. Basualdo, A. Bolopion, M. Gauthier, P. Lambert, *Sci. Rob.* **2021**, *6*, eabd3557.

[11] J. Yu, D. Jin, K. F. Chan, Q. Wang, K. Yuan, L. Zhang, *Nat. Commun.* **2019**, *10*, 5631.

[12] A. Sakes, M. van der Wiel, P. W. Henselmans, J. L. van Leeuwen, D. Dodou, P. Breedveld, *PLoS One* **2016**, *11*, e0158277.

[13] P. Koukouvinis, C. Bruecker, M. Gavaises, *Sci. Rep.* **2017**, *7*, 13994.

[14] N. F. Laubli, M. S. Gerlt, A. Wuthrich, R. T. M. Lewis, N. Shamsudhin, U. Kutay, D. Ahmed, J. Dual, B. J. Nelson, *Anal. Chem.* **2021**, *93*, 9760.
[15] a) L. G. Dai, D. J. Lin, X. D. Wang, N. D. Jiao, L. Q. Liu, *ACS Appl. Mater. Interfaces* **2020**, *12*, 57587; b) A. A. Solovev, Y. Mei, O. G. Schmidt, *Adv. Mater.* **2010**, *22*, 4340; c) A. A. Solovev, S. Sanchez, M. Pumera, Y. F. Mei, O. G. Schmidt, *Adv. Funct. Mater.* **2010**, *20*, 2430; d) W. Hu, K. A. Ishii, A. Ohta, *Appl. Phys. Lett.* **2011**, *99*, 094103.
[16] L. Rayleigh, *Philos. Mag.* **1917**, *34*, 94.
[17] a) D. Lohse, *Phys. Rev. Fluids* **2018**, *3*, 110504; b) J. R. Blake, D. M. Leppinen, Q. X. Wang, *Interface Focus* **2015**, *5*, 20150017.
[18] J. G. Santiago, S. T. Wereley, C. D. Meinhart, D. J. Beebe, R. J. Adrian, *Exp. Fluids* **1998**, *25*, 316.
[19] E. M. Purcell, *Am. J. Phys.* **1977**, *45*, 3.
[20] a) K. E. Kenyon, *J. Oper. Oceanogr.* **1998**, *54*, 343; b) V. Minsier, J. Proost, *Ultrason. Sonochem.* **2008**, *15*, 598.
[21] Z. Xiao, S. Duan, P. Xu, J. Cui, H. Zhang, W. Wang, *ACS Nano* **2020**, *14*, 8658.
[22] C. C. de Souza Silva, J. Van de Vondel, M. Morelle, V. V. Moshchalkov, *Nature* **2006**, *440*, 651.
[23] D. Vella, L. Mahadevan, *Am. J. Phys.* **2005**, *73*, 817.
[24] X. Wang, E. Bonaccurso, J. Venzmer, S. Garoff, *Colloids Surf. A* **2015**, *486*, 53.
[25] A. Huerre, M. de Corato, V. Garbin, *Nat. Commun.* **2018**, *9*, 3620.
[26] B. E. de Avila, P. Angsantikul, J. Li, M. A. Lopez-Ramirez, D. E. Ramirez-Herrera, S. Thamphiwatana, C. Chen, J. Delezuk, R. Samakapiruk, V. Ramez, M. Obonyo, L. Zhang, J. Wang, *Nat. Commun.* **2017**, *8*, 272.
[27] H. Wang, G. Zhao, M. Pumera, *J. Am. Chem. Soc.* **2014**, *136*, 2719.
[28] a) Z. G. Wu, L. Li, Y. R. Yang, P. Hu, Y. Li, S. Y. O. Yang, L. V. Wang, W. Gao, *Sci. Rob.* **2019**, *4*, eaax0613; b) C. K. Schmidt, M. Medina-Sanchez, R. J. Edmondson, O. G. Schmidt, *Nat. Commun.* **2020**, *11*, 5618; c) Z. G. Wu, J. Troll, H. H. Jeong, Q. Wei, M. Stang, F. Ziemssen, Z. G. Wang, M. D. Dong, S. Schnichels, T. Qiu, P. Fischer, *Sci. Adv.* **2018**, *4*, eaat4388.
[29] Z. H. Lin, C. Y. Gao, D. L. Wang, Q. He, *Angew. Chem., Int. Ed.* **2021**, *60*, 8750.